International Journal of Computer Information Systems and Industrial Management Applications
ISSN 2150-7988 Volume 18(2026) pp. 1-20
© Cerebration Science Publishing

https://doi.org/10.70917/ijcisim-2026-0016
Article

A Study on the Application of Three-Dimensional Scanning Data Analysis Method Based on Convolutional Neural Network in Machining Inspection

Tao Chen *

Automotive College, Sanmenxia Polytechnic, Sanmenxia, Henan, 472000, China; smxct6607@126.com

Abstract: In this paper, the mechanical workpiece point cloud data is obtained by 3D scanning technology, and the data preprocessing is realized by the extended Gaussian image clustering algorithm to align the point cloud data and other operations. Subsequently, the sliding least squares method is used to upsample the point cloud, combined with bootstrap filtering to denoise the data image and image sharpening and other processing. The improved Faster R-CNN processing detection method is designed by combining the multi-scale feature extraction structure, which improves the efficiency of machining detection by dimensionality reduction of the feature map of the previous layer, then feature extraction, and stitching the features extracted from different scale convolution kernels together. The test results show that the improved Faster R-CNN algorithm has obvious improvement in the aspects of large part size difference, occlusion, and accuracy, and can effectively solve the point cloud accurate alignment problem of local deformation of mechanical parts with strong robustness. At the same time, the performance of this model is significantly better than other comparative models in the process of target monitoring of construction machinery, and the accuracy of its AP50, AP75 and mAP indicators reaches more than 84%. In addition, the method in this paper can automatically screen the conformity of parts in machining inspection, which greatly reduces the workload.

Keywords: 3D scanning technology; Gaussian image clustering algorithm; guided filtering; multi-scale feature extraction; machining inspection

1. Introduction

Machine part manufacturing plays a critical role in industrial production, directly impacting product quality and performance. During the machining process of machine parts, defects such as cracks and inclusions, as well as issues like insufficient precision, can arise, affecting the service life and reliability of the parts [1-2]. Machine processing inspection, focused on ensuring processing quality, plays a decisive role in guaranteeing the precision of processed parts, controlling processing costs, and optimizing processing efficiency. With the rapid advancement of technology, machine processing inspection techniques are also continuously evolving and improving [3-5]. As the manufacturing industry demands increasing precision, efficiency, and consistency, traditional mechanical processing inspection methods, which typically rely on manual inspection, face challenges such as low efficiency, strong subjectivity, and limitations in precision, making it difficult to ensure measurement consistency and high efficiency, and unable to meet the current rapidly developing production demands [6-8].

With the rapid development of technologies such as artificial intelligence, integrating intelligent algorithms into mechanical processing inspection has become an inevitable trend [9]. In this context, intelligent mechanical processing inspection technology has emerged. Intelligent inspection technology offers advantages such as high inspection accuracy, high work efficiency, and resistance to human interference. While meeting the requirements for continuity, consistency, and reliability in large-scale inspections, it can free humans from harsh inspection environments and highly repetitive mechanical labor, and can adapt well to various industrial application scenarios, significantly enhancing the flexibility and intelligence of industrial product inspection processes [10-13]. The introduction of intelligent technology can also reduce errors caused by manual measurement. Intelligent mechanical processing inspection technology integrates advanced sensors, machine vision, and artificial intelligence to achieve high-precision, high-efficiency intelligent inspection of machined parts. Through deep learning and image recognition technology, it can automatically classify workpieces [14-16]. Smart manufacturing is the global trend in the manufacturing industry. The intelligent development of mechanical processing inspection technology is not only reflected in improved production efficiency and inspection accuracy; intelligent mechanical processing inspection technology is an essential component of smart manufacturing and a key technology driving the manufacturing industry toward higher levels of development [17-19].

AI-based mechanical inspection uses deep learning algorithms to quickly and accurately identify defects or precision issues, significantly improving inspection efficiency and accuracy. Among these, convolutional neural networks are a representative type of deep learning algorithm. The advantages of this algorithm are more evident when the network input is a multidimensional image, allowing the image to be directly input into the network, avoiding the complex feature extraction and data reconstruction processes in traditional recognition algorithms. The convolutional network is a specially designed multi-layer perceptron for recognizing two-dimensional shapes. This network structure exhibits high invariance to translation, scaling, rotation, or other forms of deformation, enabling comprehensive feature extraction, remote control, and high efficiency in mechanical processing inspection [20-23].

In the field of mechanical processing, the development of quality inspection technology has evolved from traditional tools such as vernier calipers and micrometers to modern contact and non-contact inspection methods, reflecting the increasing demands for precision, efficiency, and diversity in mechanical processing inspection. Current mechanical processing inspection processes are primarily divided into contact-based and non-contact-based inspection methods. As described in Reference [24], in mechanical inspection, non-contact-based inspection methods, which are based on optical principles, offer advantages such as faster inspection speeds, better capture of mechanical surface information, and higher data point density compared to contact-based methods, making them more widely adopted.

In contact measurement processes, coordinate measuring machines are the most modern form of contact measurement, obtaining key geometric parameters of parts by contacting the surface of the object being tested with a probe [25]. Reference [26] uses a coordinate measuring machine to capture data points on the gear surface during gear processing, combines non-uniform rational B-spline surfaces for fitting, constructs a three-dimensional model of the gear surface, analyzes characteristic points and original data points, and detects the accuracy of the gear surface in the form of comparison-error compensation-re-comparison. Reference [27] describes a contact-type thread tester for defect detection in thread processing. The instrument uses a camera to identify thread hole dimensions, based on which it automatically adjusts quality inspection related to optimal torque, making it less susceptible to noise interference.

In non-contact detection, the most typical methods for non-contact detection in mechanical processing are laser triangulation and machine vision measurement. Reference [28] employs laser triangulation combined with a designed threshold sub-pixel grayscale-gravity extraction algorithm for online measurement of threads and screw rotors, achieving higher accuracy than the basic laser triangulation method. Literature [29] employs laser scanning technology to obtain three-dimensional point cloud data of parts, applies the Point Cloud Library (PCL) for data denoising, and combines segmentation techniques to construct a three-dimensional data model. By measuring the deviation between the scanned point cloud and the designed point cloud, it detects surface dimensions and deviations of mechanical parts in industrial applications. Reference [30] designed an automatic online non-contact measurement system for thread detection using eye-tracking machine vision and morphological techniques. The system incorporates multiple image processing and machine vision technologies to extract and analyze thread images and contours, with a detection error of ±6 micrometers. Reference [31] invented a visual system-based method for measuring the roughness of machined surfaces such as molds, enabling rapid roughness detection of parts with complex geometric shapes. Literature [32] employs analytical modeling and numerical simulation to acquire and simulate the impact sound of bolt connections, combined with acoustic testing, to achieve effective detection of bolt loosening. Literature [33] utilizes high-definition cameras to capture images of mechanical components, incorporating the Grad-CAM (Gradient-weighted Class Activation Mapping) algorithm for defect identification in images, thereby accelerating the speed of quality inspection while enhancing detection accuracy. Literature [34] designed a machine vision system supported by a multi-task convolutional neural network algorithm to detect defects on bearing roller surfaces. This was achieved by extracting features from the bearing surface, classifying and calculating defects, and comparing them to determine compliance with standards.

In this paper, a three-dimensional point cloud data alignment method is proposed and applied to the mechanical workpiece deformation identification. The 3D laser point cloud data of mechanical workpiece is collected by 3D scanning technology, and after clustering and inverse Gaussian mapping, the obtained optimal Gaussian point cloud clusters are converted into 3D solid point clouds to complete the point cloud alignment of laser scanning of mechanical workpiece. After that, the acquisition of point cloud data, preprocessing, and image denoising and image sharpening are introduced, followed by the introduction of the Mask R-CNN algorithm used in this paper. On the basis of Faster R-CNN, the RPN network that generates the anchor point enclosing frame in the original Faster R-CNN is retained, and improvements are made in terms of the base network and the loss function in the feature extraction stage, in order to improve the detection accuracy and detection speed of the model. Finally, the effect of the improved Mask R-CNN 3D scanning data analysis method applied to machining inspection is analyzed.

2. Convolutional Neural Network-Based Method for Analyzing 3D Scanning Data

2.1. Acquisition and Processing of 3D Laser Scanning Deformation Point Cloud Data

2.1.1. 3D Laser Scanning Point Cloud Data Acquisition

In this paper, laser triangulation is used to complete the work of 3D laser data scanning [35] of mechanical workpieces. Through the laser scanner laser line to the workpiece, and then use the sensor to collect the reflected laser line, so as to obtain the 3D laser point cloud data of the workpiece. Mechanical workpieces have small deformation variables, and small changes in mechanical workpieces can be quickly sensed with the help of laser displacement sensors, which can be avoided from environmental constraints due to their small form factor and ease of installation. The distance is calculated based on the laser round-trip time, and the 3D coordinates (x, y, z) of each point are obtained, and the coordinate calculation formula is:

$$\begin{cases} x = Sc\cos\lambda\sin\delta \\ y = S\cos\lambda\cos\delta \\ z = S\sin\sigma \end{cases} \tag{1}$$

where S is the distance between the sensor and the target, λ is the instantaneous laser horizontal angle δ is the laser vertical angle σ is the laser emission angle.

The three-dimensional coordinates of each point are assembled to obtain the mechanical workpiece surface point cloud data, but by the interference of environmental factors, there is noise in the data, which needs to be further processed by noise reduction.

2.1.2. Point Cloud Data Missing Matching Algorithm Design

As the 3D laser point cloud data contains a large amount of noise data, it is difficult to extract it directly. Therefore, it is necessary to carry out preprocessing operations, mainly including point cloud alignment, point cloud filtering and point cloud thinning and other steps, to reduce the amount of data while effectively eliminating the influence of noise.

There are missing point clouds in the laser point clouds of mechanical workpieces obtained from scanning. In this paper, the ICP algorithm [36] is used for fine matching, which not only avoids the dependence of the algorithm on the initial position of the point cloud, but also enhances the matching accuracy of the missing point cloud.

The normal vectors of each point in the laser point cloud of mechanical workpiece can provide the orientation information of the surface of mechanical workpiece, which is important for determining the surface topology of mechanical workpiece, workpiece machining, assembly and inspection, and can provide potential spatial information for the clustering of the laser point cloud data of mechanical workpiece.

Suppose that a point $Q_i(x_i, y_i, z_i)$ is fitted to the plane equation of the point using the least squares method, the sum of squares of the deviations of the equation is:

$$\alpha = \sum_{i=1}^{n}[(ex_i + fy_i + g) - z_i]^2 \tag{2}$$

where (e, f, g) denotes the normal vector of the point in the plane, which varies with the position of $Q_i(x_i, y_i, z_i)$. When α takes the smallest value, the value of the corresponding normal vector (e, f, g) is determined. Coarse matching is performed after the clustering process so that the Gaussian point cloud clusters can correspond to the original point cloud. The point cloud position difference is:

$$d = \gamma \sum_{i=1}^{n} (v_i - v_i^{'})^2 + \eta \sum_{i=1}^{n} (m_i - m_i^{'})^2 \tag{3}$$

where γ, η denotes the weight parameter, v denotes the Gaussian point cloud cluster volume, $v^{'}$ denotes the original point cloud cluster volume, m denotes the Gaussian point cloud cluster vector modulus, and $m^{'}$ denotes the original point cloud cluster vector modulus. The Gaussian point cloud cluster is optimal when the value of d is smallest.

The obtained optimal Gaussian point cloud clusters are inversely Gaussian mapped and thus converted into 3D solid point clouds. In this paper, the following descriptive function is used to complete the query of the corresponding points so as to realize the coarse matching:

$$N = \alpha \sum_{i=1}^{n} (p_i - p_i^{'})^2 + \beta \sum_{i=1}^{n} [(\overline{t_i} - \overline{t_i}^{'})^2 + (t_i - t_i^{'})^2]^2 \tag{4}$$

where p denotes the point-to-center-of-mass distance of the inverse Gaussian point cloud $p^{'}$ denotes the point-to-center-of-mass distance of the 3D solid point cloud $\overline{t}$, t denotes the mean curvature and Gaussian curvature, $t^{'}$, $\overline{t_i}^{'}$ denotes the transformed mean curvature and Gaussian curvature respectively and β denotes the divergence angle. In this paper, the extended Gaussian image clustering algorithm combined with the ICP alignment algorithm is used to realize the matching of mechanical point cloud data, on the basis of which the deformation of the workpiece is further identified.

2.2. Machining Point Cloud Data and Image Generation Processing

2.2.1. Point Cloud Data Processing

(1) Point cloud interpolation

In point cloud data acquisition, the data quality is affected by factors such as equipment as well as scanning speed, which makes it easy to have insufficient sampling density. In this paper, sliding least squares [37] (MLS) is used to upsample the point cloud.

(2) Point cloud projection

The projection of point cloud refers to the projection of the preprocessed point cloud data, which is converted into a visualized planar unfolding map for subsequent operations. Currently, the unfolding projection of the point cloud includes: planar projection, spherical projection, ellipsoidal projection, and cylindrical projection.

Planar projection is only applicable to relatively flat point clouds; spherical projection is to transfer the original point cloud to a unified spatial coordinate system, and then the sphere as a medium to project the coordinates (X_i, Y_i, Z_i) to get the corresponding two-dimensional coordinates (x_i, y_i) which is more applicable to the surrounding type of scattered or orderly point cloud. Ellipsoidal projection is to project the point cloud onto the ellipsoid along the center of the ellipsoid.

(3) Point cloud mapping

After the completion of the point cloud projection needs to image, it is considered to complete the point cloud to obtain the image of the complete operation. At present, the conversion from 3D point cloud to 2D point cloud has been realized. There are two ways to realize the final mapping operation: converting the existing point cloud into a matrix; and pixel mapping. Conversion of point cloud to matrix: Each point in a 2D point cloud is regarded as an item in the matrix, a point means that the value of the matrix item is 1, and no point means 0. At this point, the planar point cloud can be directly regarded as a 2D image. The advantage is that the image can be generated efficiently, but there is a problem of resampling. In the three-dimensional point cloud stage, the data has been resampled to improve the density of data points. Therefore, no further resampling is required at this stage. Pixel Plotting: This operation will make heavy use of the Point and Scalar structures; the Point structure represents the points corresponding to x and y. The Scalar is heavily used to pass pixel values. Scalar is heavily used to pass pixel values. This is described in more detail in a later section.

2.2.2. Image Processing

(1) Image denoising

Before an image is processed, there is a certain level of noise, however, the noise prevents the recognition of the target and affects the results of the experiment. Therefore, image denoising is used to reduce the noise in the image, which reduces the impact of noise and improves the recognition accuracy. Mean filtering and Gaussian filtering are more mature and classical image processing methods, and compared with them, bootstrap filtering is more effective. Therefore, in this paper, bootstrap filtering is selected for image denoising operation:

$$q_i = \sum_j W_{ij}(I) p_j \tag{5}$$

where I is the bootstrap image, p is the input image to be denoised, q is the output image, and W is the weights determined based on the bootstrap image II. W is denoted as:

$$W_{ij}(I) = \frac{1}{|\omega|^2} \sum_{k:(i,j)\in\omega_k} (1 + \frac{(I_i - \mu_k)(I_j - \mu_k)}{\sigma_k^2 + \varepsilon}) \tag{6}$$

where ω_k is the k th kernel function window, μ_k is the mean of the points within the window, I_i and I_j are the values of the neighboring points, σ_k is the variance of the corresponding points within the window, and ε is a penalty value. As an adaptive weight filter, we can analyze that I_i and I_j are dissimilar in sign when they are on both sides of the boundary, $(I_i - \mu_k)$ and $(I_j - \mu_k)$ are identical otherwise, and therefore the weight values are different.

(2) Image sharpening

In order to change the effect of unclear image, sharpening can increase the contrast between the edge and the surrounding to make the picture clear. Image sharpening is divided into differential method and high pass filtering method.

The first type, the airspace differential method. The image is not clear because it is subjected to integration or averaging operation, therefore, the method is to do the opposite operation and perform differential calculation to make the image clear.

The commonly used first order differential and second order differential are shown in the following equations:

$$\frac{df}{dx} \to f_n^{'} = f(n+1) - f(n) \tag{7}$$

$$\frac{d^2 f}{dx^2} \to f_n^{''} = f(n+1) + f(n-1) - 2f(n) \tag{8}$$

First-order and second-order differencing can be used to solve for variations in parts of the image such as edges. After the differential sharpening process, $g(n)$ is represented:

$$g(n) = f(n) + [-f^{''}(n)] \tag{8}$$

where $f(n)$ denotes the current blurrier signal itself, $-f^{''}(n)$ denotes the edge information extracted by differentiation, and the two are superimposed to generate the sharpening enhancement. Therefore, the edge detection operators to be used in this paper need to achieve the enhancement effect in different directions.

The directionless sharpening is divided into the following operators: the Roberts operator, the Sobel operator, the Prewitt operator, and the Laplace operator.

Roberts operator is called cross-differential operator, simple algorithm, weak ability to extract information, suitable for processing simpler images. Laplacian operator satisfies the effect of enhancement in different direction edges.

Laplacian operator:

$$V^2 f = \frac{\partial^2 f}{\partial x^2} + \frac{\partial^2 f}{\partial y^2} \tag{10}$$

The above formulas are Laplace operator expressions.

The sharpening formula is:

$$g(m,n) = f(m,n) + \alpha[-\nabla^2 f(m,n)] \tag{11}$$

When the value of α is different, the sharpening effect is different. The larger the value of α, the more pronounced the sharpening effect and the clearer the edges.

However, the Laplace operator is sensitive to noise and produces double edges for some edges in the graph. So smoothing needs to be done first. However, this paper needs to seek better image sharpening methods.

In the second category, frequency domain high pass filtering method. Another type is when observing the frequency domain, it is found that the reason for image unsharpness is the recession of information in the high frequency band. So the problem is solved by using high-frequency filtering to weight the high frequencies.

After the Fourier transform will be converted to the original image frequency domain, high-pass filtering in the frequency domain, after the Fourier inverse transform; and then superimposed with the original image can be obtained after sharpening results.

The specific formula is expressed as:

$$y(n,m) = x(n,m) + \lambda z(n,m) \tag{12}$$

where $x(n,m)$ is the input, $y(n,m)$ is the output, and $z(n,m)$ is the correction signal. A high-pass filtering operation is performed on x, and λ plays a scaling role, which will be used to control the degree of enhancement.

In conventional USM, $z(n,m)$ is obtained as:

$$z(n,m) = 4x(n,m) - x(n-1,m) - x(n+1,m) - x(n,m-1) - x(n,m+1) \tag{13}$$

In comparison, the variation of the parameter λ can dynamically change the sharpening results. In the smooth part of the image transformation and at the edges with high contrast, λ takes a smaller and appropriate value, respectively; while in the medium contrast, a larger λ indicates that there is a focus on maximizing the sharpening of that part.

2.3. Improved Faster R-CNN Algorithm

2.3.1. Multi-Scale Feature Extraction

Part size disparity is a frequently encountered problem in the target detection of mechanical parts, and it is also a major difficulty in the current detection task. In the convolution process, the size of the convolution kernel affects the extraction of local and global information of the image. The multi-scale feature extraction structure (MFES) in this section employs different scales of convolution and pooling operations in the same feature extraction layer, which fully preserves both the detail information of the original machine part image and the global spatial properties in the whole image.

In this section, in the original Faster R-CNN [38] network structure, the 6th and 12th layers are removed, and the two 3x3 convolutional layers with dimensions of 256 dimensions and 512 dimensions are removed, while in the network structure after the removal of the convolutional layers, the 9th and 11th layers are added into the multi-scale feature extraction structure, respectively. After calculation, the number of parameters reduced in each of the two convolutional layers is 599024 in layer 6 and 2300342 in layer 12, and the parameter reduction of the whole network structure after improvement is 2903155, while the number of parameters increased in the two layers of multiscale feature extraction structure is 470020, and the total amount of increase is 940054. Therefore, the whole network structure after improvement is 2903155. Faster R-CNN network structure has a parameter reduction of 2009890.

2.3.2. Cascade Feature Map Structure

In this paper, USM algorithm which introduces parametric thresholding in frequency domain high pass filtering method is used for image sharpening. Both one layer and this layer are convolved with convolution kernels of the same size and the same dimension. If i represents each layer in the network structure, x_i denotes the input of each layer, and y_i denotes the output of each layer, i.e., the output feature maps of each layer, then the input of the 10th layer is computed as:

$$x_{10} = H(y_2, y_4, y_6, y_8, y_9) \tag{14}$$

In the above equation, $H(y_2, y_4, y_6, y_8, y_9)$ denotes that the feature maps of the outputs of the 2nd, 4th, 6th, 8th, and 9th layers are cascaded after the pooling operation, i.e., there are a total of 5 inputs to the 10th convolutional layer.

Without making any changes to the network, the size of the feature map after passing to layer 9 is 14 × 14, so it is necessary to pool the size of the feature map of the previous layer to a size of 14 × 14 to cascade with the convolutional feature map of layer 9, and the pooled convolutional kernel is given by:

$$k_i = \frac{y_i}{14} \tag{15}$$

where i denotes the ith layer of the network structure, y_i denotes the size of the ith layer feature map, and k_i denotes the size of the pooled convolution kernel in the ith layer, i.e., the ratio of the feature map in the ith layer to the feature map in the 9th layer.

2.3.3. Joint Exclusion Loss Function

Considering the loss generated by the occlusion problem into the mechanical parts detection is a very worthy of attention, this paper in the original Faster R-CNN network classification and regression loss function, based on the exclusion loss proposed a joint exclusion loss function for mechanical parts target detection, to realize the three kinds of loss monitoring at the same time, to improve the detection accuracy due to the target occlusion problem caused by interference problems The problem of interference in detection accuracy due to target occlusion is improved.

The similarity with pedestrian detection is that pedestrian detection considers the relationship between the target person and non-target person or other non-target objects, while parts consider the relationship between the target parts and similar parts or non-similar parts. The joint exclusion loss function is:

$$L = L_S + \lambda L_R \tag{16}$$

where L_S denotes the sum of the four parts of the classification and regression loss in the RPN part and the classification loss and regression loss in the FastR-CNN part of the original FasterR-CNN network structure, and L_R denotes the rejection loss function, which mainly consists of three parts, i.e.,:

$$L_R = L_{Attr} + \alpha L_{\mathrm{Re}pGT} + \beta L_{\mathrm{Re}pBoz} \tag{17}$$

where the coefficients α and β act as weights to balance the auxiliary loss.

The first sub-module L_{Attr} is the attraction term that makes the prediction frame and the target frame on the match as close as possible, i.e., the SmoothLl loss aims to make the regression target close to the true target:

$$L_{Attr} = \frac{\sum_{P \in \mathrm{P}_+} Smooth_{L1}(B^P, G^P_{Attr})}{|\mathrm{P}_+|} \tag{18}$$

where $P = (l_p, t_p, w_p, h_p)$ and $G = (l_G, t_G, w_G, h_G)$ are the candidate region proposal bounding box and the truth bounding box, and are represented by the coordinates of their upper-left points and their heights, widths, respectively denotes. $\mathrm{P}_+ = \{P\}$ (is the set of all positive candidate region suggestions); $G = \{G\}$ is the set of all truth-value bounding boxes in a picture, and B^p is the prediction box for regression from suggestion P:

$$G^{p}_{Attr} = \arg\max{}_{GeG}\, IoU(G,P) \tag{19}$$

The second sub-module L_{RepGT} is the exclusion term that makes the prediction frame and the surrounding target frame as far away from each other as possible, i.e., the goal is to make the prediction frame as far away as possible from the second-largest truth-valued border that overlaps it:

$$L_{RepGT} = \frac{\sum_{P \in \mathrm{P}_+} Smooth_{kn}(IoG(B^{P}, G^{P}_{Rep}))}{|\mathrm{P}_+|} \tag{20}$$

where $\sigma \in [0,1)$ is the smoothing parameter that adjusts the sensitivity of the repulsive force to outliers:

$$Smooth_{b_n} = \begin{cases} -\ln(1-x) & x \le \sigma \\ \dfrac{x-\sigma}{1-\sigma} - \ln(1-\sigma) & x > \sigma \end{cases} \tag{21}$$

$$IoG(P,G) = \frac{area(P \cap G)}{area(G)} \tag{22}$$

$$G^{p}_{Rep} = \arg{}_{GeG \setminus \{G^{P}_{Aer}\}}\, IoU(G,P) \tag{23}$$

The more the candidate region proposal tends to overlap with non-target truth frame objects, the more the RepGT loss penalizes the bounding box regressor, thus effectively preventing the bounding box from moving to neighboring non-target objects.

The third sub-module L_{RepBOX} is the rejection term, non-extremely large value suppression is an indispensable post-processing step in the vast majority of detection frameworks, in order to reduce the detector's sensitivity to the non-extremely large value suppression, the RepBox loss is then proposed to exclude the proposed frames coming from differently specified targets.The RepBox loss can be calculated as:

$$L_{\mathrm{RepBer}} = \frac{\sum_{i \ne j} Smooth_{kn}(IoU(B^{P_i}, B^{P_j}))}{\sum_{i \ne j} \text{í}\,[loU(B^{P_i}, B^{P_j}) > 0] + \text{ò}} \tag{24}$$

where í is a constant function and ò is a very small constant to prevent the denominator from being zero.

3. Application of Three-Dimensional Scanning Data Analysis Methods to Machining Inspection

3.1. Point Cloud Fine Alignment Test

Comparison tests of classical ICP, Huber ICP and the algorithm of this paper were designed. The test scenario species, the size of the rectangular model is 8mm × 7mm × 3mm, and the sampled point cloud of this model contains 9563 points. Random noise with a standard deviation of 0.02mm is added to the sampled point cloud to simulate the random measurement error of the 3D scanner. In this paper, 2 observation points A (located on the plane) and B (located in the raised part) are set to represent the non-processing error point and processing error point respectively, and the actual deviation of point B is 0.95 mm.

The results of the point cloud fine alignment test are shown in Fig. 1, where (a) ~ (d) represent the weighted value, residual, residual standard deviation and residual mean, respectively. As can be seen from the figure, the classical ICP does not carry out weight selection calculation, so the weights of points A and B are always 1. Comparing the Huber ICP and this paper's alignment algorithm, the Huber ICP weights of observation point B, which is located on the bulge, are 0.2093, while the weights of this paper's alignment algorithm are reduced to 0.0000, which can be seen that this paper's alignment algorithm can give smaller weights and eliminate more error points than Huber ICP. It can be seen that the alignment algorithm in this paper can give smaller weights to the error points than Huber ICP, which can eliminate the influence of the error points on the alignment results, and the deviation between point B and the model at the end of the iteration is closer to the actual error value.

The standard deviation of the residuals after convergence is still close to 0.1776 mm. Comparing the Huber ICP and this paper's alignment algorithm, the Huber ICP has not been able to reduce the weights of the error points completely, and the residuals of the Huber ICP still have a large impact on the alignment until convergence, which results in the standard deviation of the residuals being close to 0.0912 mm; whereas the standard deviation of the residuals of this paper's algorithm is only 0.0912 mm after convergence. The standard deviation of the residuals is only 0.0315mm, which is comparable to the random error added in the sampled point cloud (standard deviation of 0.03mm). The average value of the residuals of this alignment algorithm is always lower than that of Huber ICP, and the test shows that the alignment method proposed in this paper can greatly improve the alignment accuracy, and the final alignment residuals are comparable to the random noise level of the point cloud itself, and the alignment method can overcome the adverse effects of processing errors on the alignment calculation, and has strong robustness.

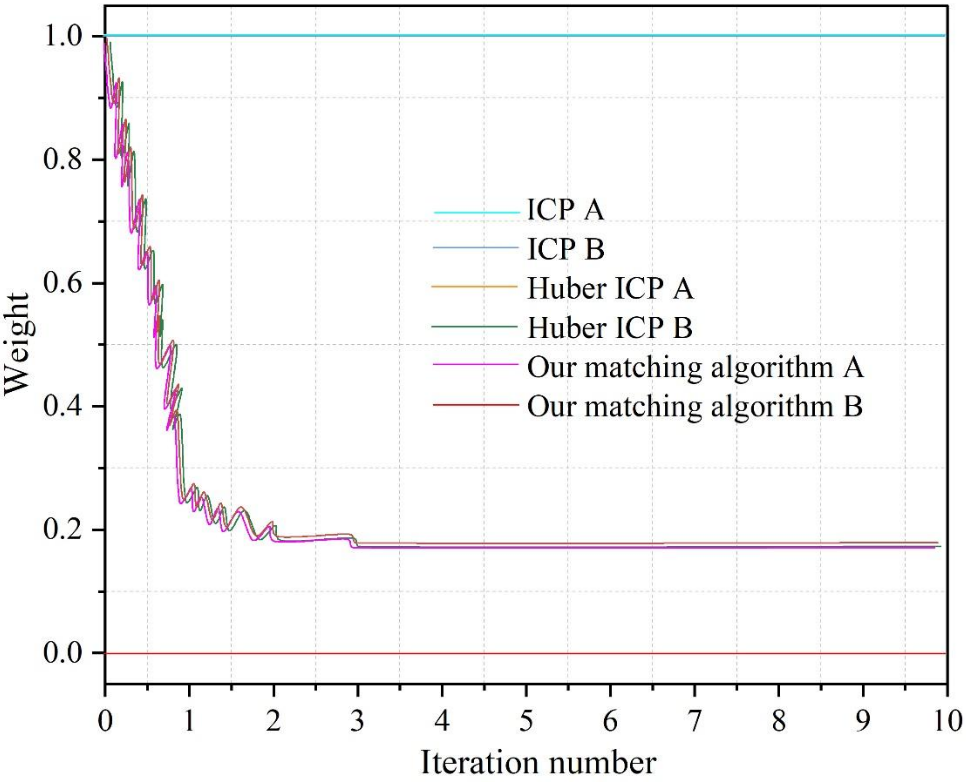

(a) Weight

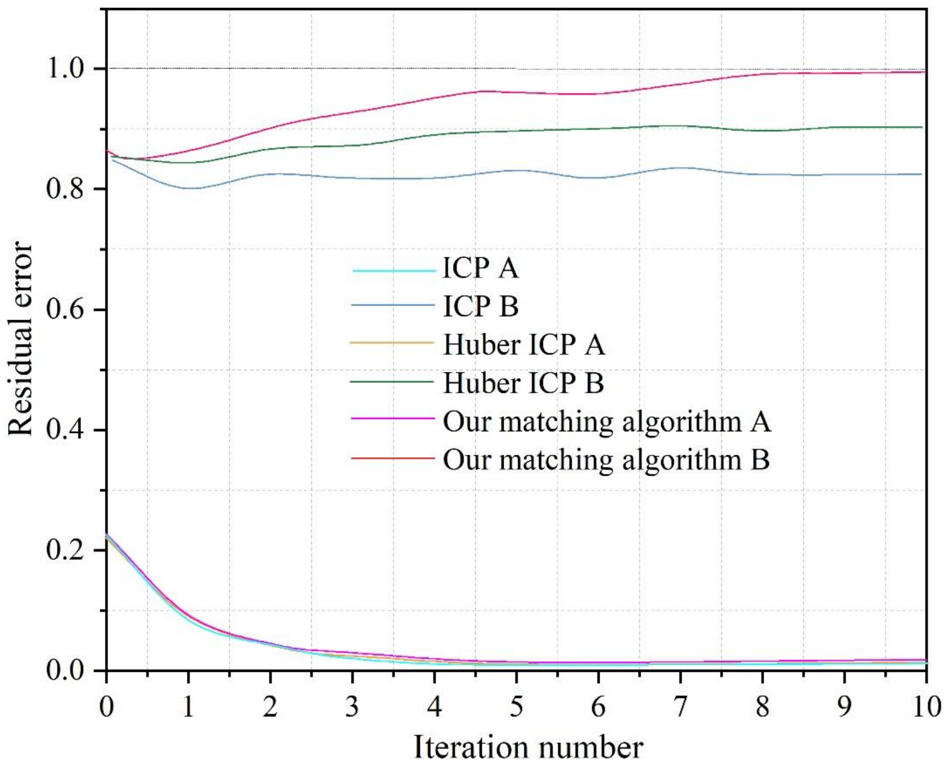

(b) Residual error

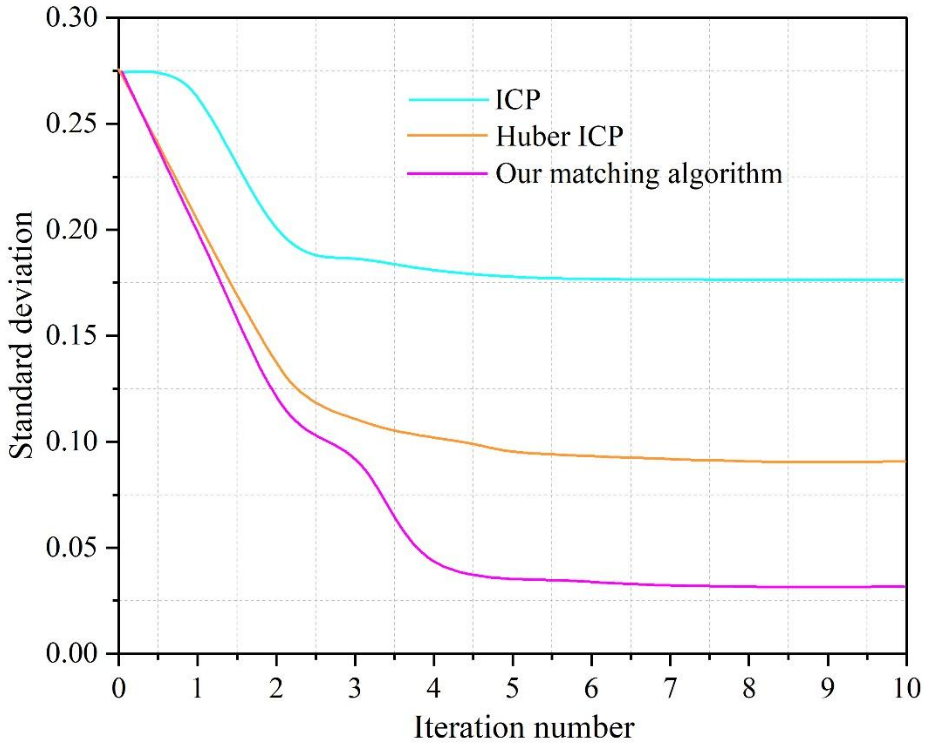

(c) Standard deviation

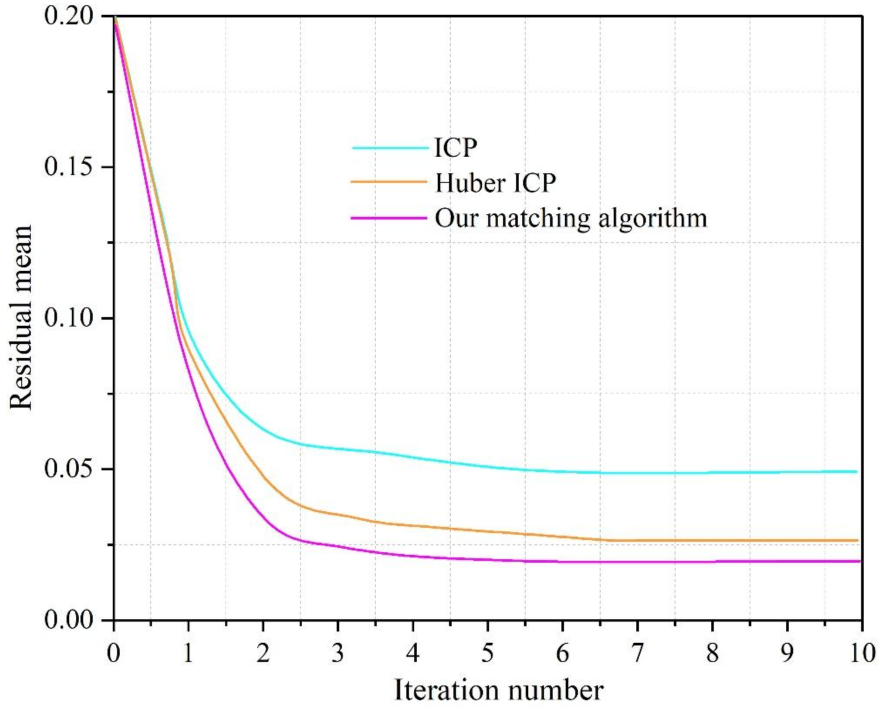

(d) Residual mean

Figure 1. The results of the precise and accurate test of the dot cloud.

3.2. Multi-Scale Feature Fusion Target Monitoring Method for Construction Machinery

3.2.1. Experimental Environment and Parameter Settings

(1) Experimental dataset

The dataset images used in this paper are taken from the web and the field and contain a total of 1410 targets in various scenarios, including 400 tower crane targets, 500 excavator targets and 510 crane targets. The annotation tool used in this paper is labelling.

(2) Network training and optimization parameters

The training of the network model uses Mini batch small batch training, the number of sample images in each batch is 2, and the use of migration learning to train the backbone network in order to speed up the training speed of the network model, and the training uses the SGB optimizer. In the training and optimization settings of the network model algorithm in this paper, the initial training learning rate is 0.002 and the number of iterations is 10. In the setup parameters, the initial learning rate is 0.002, the weight decay coefficient is 0.005, the momentum coefficient is 0.85, the learning rate adjustment multiplier is 0.35, and the step size is 4.

3.2.2. Evaluation indicators

Evaluating the performance of target detection algorithms is usually done using precision and recall, AP and mAP.

(1) Precision and Recall

In a target detection task, it is necessary to calculate how many real targets are detected and what percentage of all targets are detected, and this requires precision rate and recall rate to evaluate. Precision rate and recall rate are also known as detection accuracy rate and detection completeness rate, which are defined as:

$$Precision = \frac{TP}{TP + FP} \tag{25}$$

$$Recall = \frac{TP}{TP + FN} \tag{26}$$

where, TP true case, in target detection also denotes the number of predicted frames with the true frame $IOU > 0.5$, FP false positive case, denotes the number of predicted frames with the true frame $IOU \leq 0.5$, TN true counterexample, and FN false counterexample, denotes the number of true frames that are not detected.

(2) AP and mAP

After precison and recall are calculated, mAP is the average precision mean for all categories:

$$AP = \frac{1}{Q} \sum_{r \in (0,1)} P(r) \tag{27}$$

$$mAP = \frac{AP}{N} \tag{28}$$

where $P(r)$ denotes the maximum value of precison when $recall > r$, Q denotes the number of specific values taken by r , and N denotes the number of categories. mAP takes a value in the range of 0 to 1, with higher values representing better detection performance of the network model.

3.2.3. Analysis of Experimental Results

(1) Experimental results of the alignment algorithm in this paper

In this paper, according to the above experimental environment, parameters and data sets for training and experiments, Figure 2 shows the results of the training loss and learning rate change of the alignment algorithm in this paper. From the figure, it can be seen that through the adjustment of the learning rate, the Loss value gradually decreases during the training process, and when the iteration reaches a certain number of times, the Loss value is infinitely close to 0, indicating that the training effect of the network model is getting better and better.

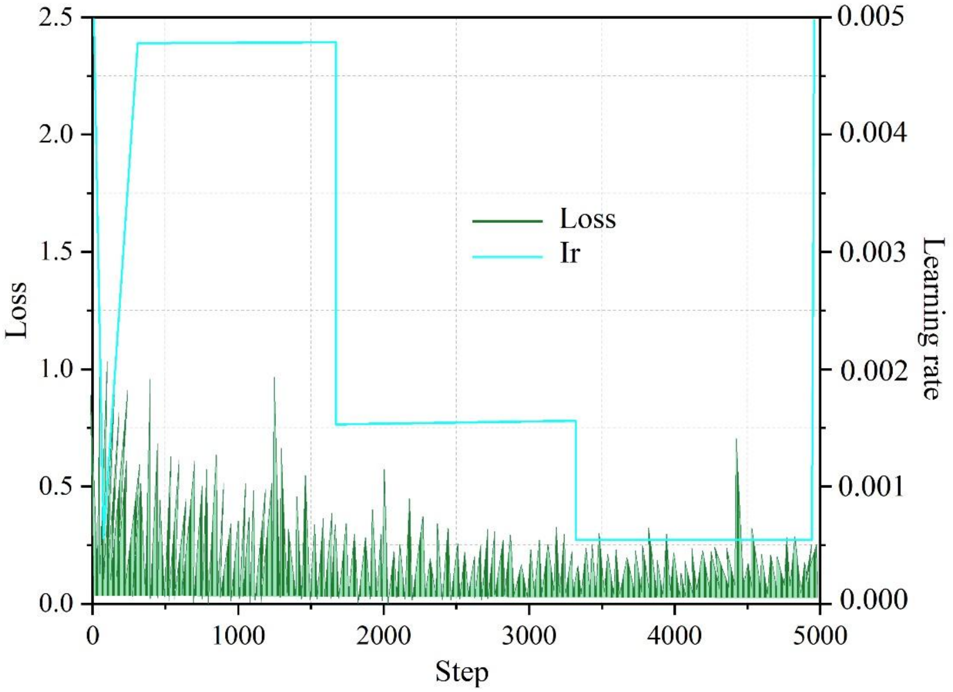

Figure 2. The training loss and learning rate of the model.

The average accuracy of different algorithms versus iteration is shown in Fig. 3. The comparison of the evaluation metrics of the experimental results of the different network models is shown in Fig. 4. From the figure, it can be seen that the values of AP50, AP75 and mAP obtained by Huber ICP when trained with the dataset of this paper and validated on the validation set are 87.99%, 69.64% and 78.68%, respectively. While the three metrics of the alignment algorithm in this paper reached 95.52%, 84.98% and 90.41% respectively. Compared with other target detection algorithms, all the indexes of this paper's alignment algorithm are much improved. Compared with Huber ICP, the detection effect of this paper's alignment algorithm is more ideal, which also proves that this paper's alignment algorithm is more suitable for the problem scenarios in this paper, and it can effectively solve the difficulties in the detection of 3D scanning data analysis methods in machining, and it has better detection accuracy and robustness than Huber ICP algorithm.

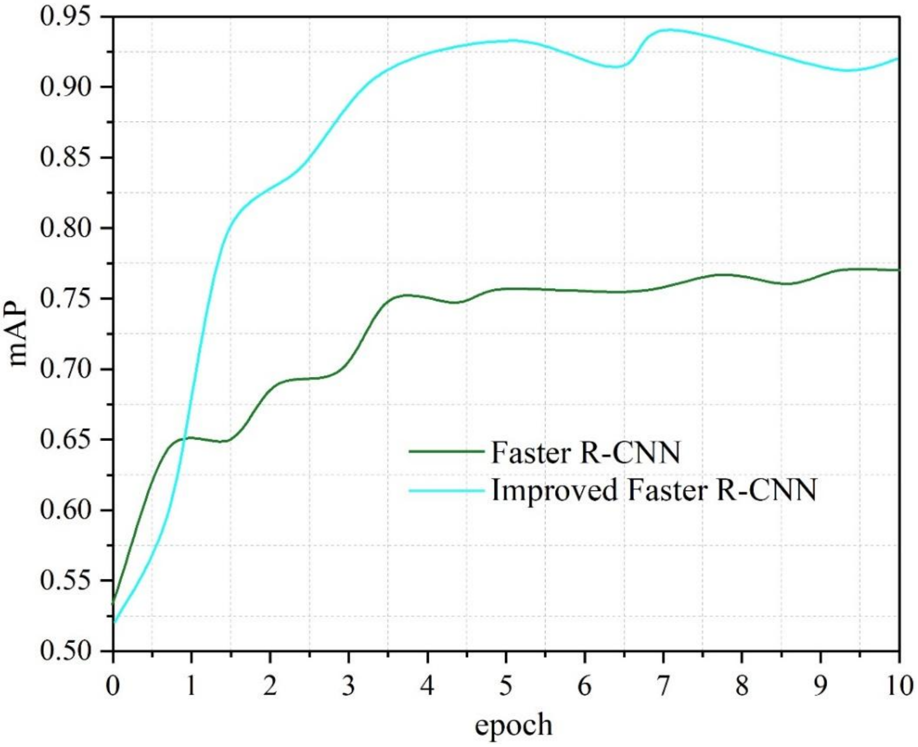

Figure 3. The average accuracy and iterative relationship of different algorithms.

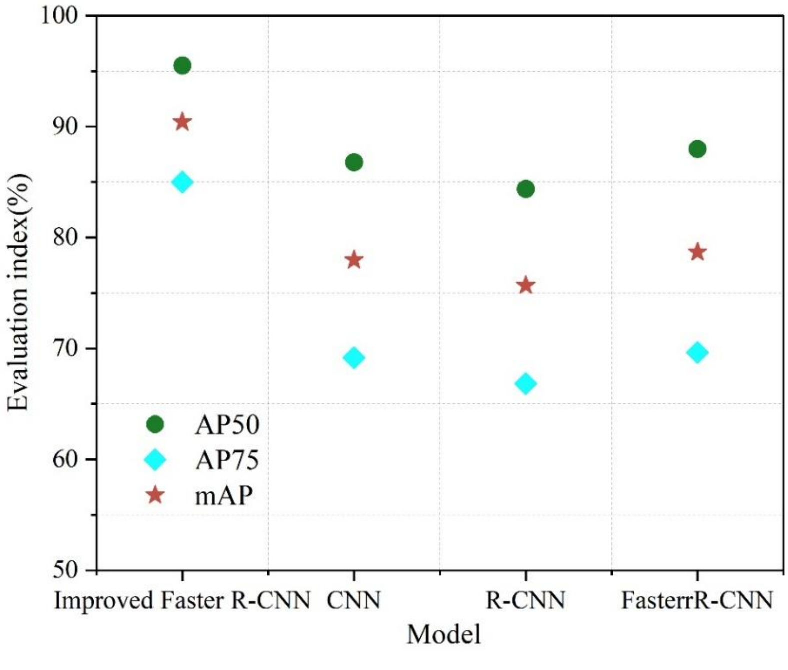

Figure 4. The experimental results of different network models were compared.

(2) Comparison of experimental results under different improvements

In this paper, relevant experimental comparisons are also carried out for each part of the proposed improvements, and the experimental results of mAP comparison under different improvements are shown in Table 1. As can be seen from the table, the mAP of Huber ICP network is 78.91% under the dataset of this paper, and after adjusting the extraction structure to multi-scale MFES, the mAP is improved by 3.3%; after adding RPN on top of MFES, the mAP is improved by another 2.65%; and after the introduction of parameter-thresholding USM algorithm, the mAP is improved by another 2.13%. Afterwards, after continuing to modify the anchor box aspect ratio of the RPN network through the joint exclusion loss function RepGT, the mAP is improved by another 1.22%, and finally, after introducing the RepBox loss to exclude the suggestion boxes from different specified targets, the mAP reaches 91.32%, which fully proves that the improvement of the alignment algorithm in this paper is effective.

Table 1. Different improved maps compare experimental results.

Main dry network	RPN	The feature path aggregation network PRPN	K-means anchor frame adjustment	RepBox	mAP
VGG16	—	—	—	—	78.91
MFES	—	—	—	—	82.21
	√	—	—	—	84.86
	√	√	—	—	86.99
	√	√	√	—	88.21
	√	√	√	√	91.32

(3) Comparison of experimental results for different anchor frame aspect ratios

For the improvement of adjusting the anchor frame aspect ratio using RepBox algorithm, this paper also did several sets of experiments on it, and the detection mAP results under different anchor frame aspect ratios are shown in Table 2. From the table, it can be concluded that the width-to-height ratio of the anchor box is not the more the better. The most suitable anchor frame aspect ratios for the problem scenarios in this paper are 1:1.5, 1:1.8, and 1.8:1, and with the increase of the number of aspect ratios, the detection accuracy mAP value of the model becomes lower. Comparing the first and second rows of the table, it can be seen that compared to the default anchor frame aspect ratio of the Huber ICP, after adjusting the anchor frame aspect ratio using the RepBox loss function, the detection accuracy mAP of the network model is improved by 4.43% compared to the initial Huber ICP. When the alignment algorithm in this paper uses the default anchor frame aspect ratio for target detection, there are multiple or missed detections, and the predicted target frames do not fit the target well. After adjusting the anchor frame aspect ratio using the RepBox clustering algorithm, the target detection is more accurate and the target frame fits the target better.

Table 2. Test map results of different anchor frame wide high ratio.

Network subject	Anchor frame adjustment	mAP (%)
MFES+USM+RepBox	1:1.2, 1:2.5, 2.5:1	87.48
	1:1.5, 1:1.8, 1.8:1	91.91
	1:1.5 1:1.4 1:1.3 1.7:1	87.86
	1:1.8 1:1.3 1:1.4 1.8:1 1.3:1	82.79

3.3. Normal Distribution Hypothesis Testing

In order to verify the correctness of the error test and machining accuracy evaluation method, four groups of sampled point clouds are used to compare and detect with the original model. The results of the model comparison test are shown in Fig. 5, where (a)~(d) represent point clouds 1~4, respectively.The problem of machining error is simulated by adding deformation, and different degrees of random noise are added to simulate the problem of machining accuracy:point cloud 1 has no deformation, and the random noise with standard deviation of 0.01mm is added, and its distance deviation should be normally distributed to simulate a qualified part; point cloud 2 has a large bulge, and the maximal deviation is

1.55mm, add a standard deviation of 0.04mm of random noise, its distance deviation does not meet the normal distribution, can simulate the manufacturing process in the presence of large processing errors in the parts; point cloud 3 has a uniform distribution of fine deformation, the maximum deviation of 0.28mm, add a standard deviation of 0.03mm of random noise, its distance deviation does not meet the normal distribution, can simulate the artificial not easily detected with a Point cloud 4 has no deformation, adding random noise with a standard deviation of 0.099mm, its distance deviation obeys the normal distribution but has a larger standard deviation, so it can simulate parts with rough processing.

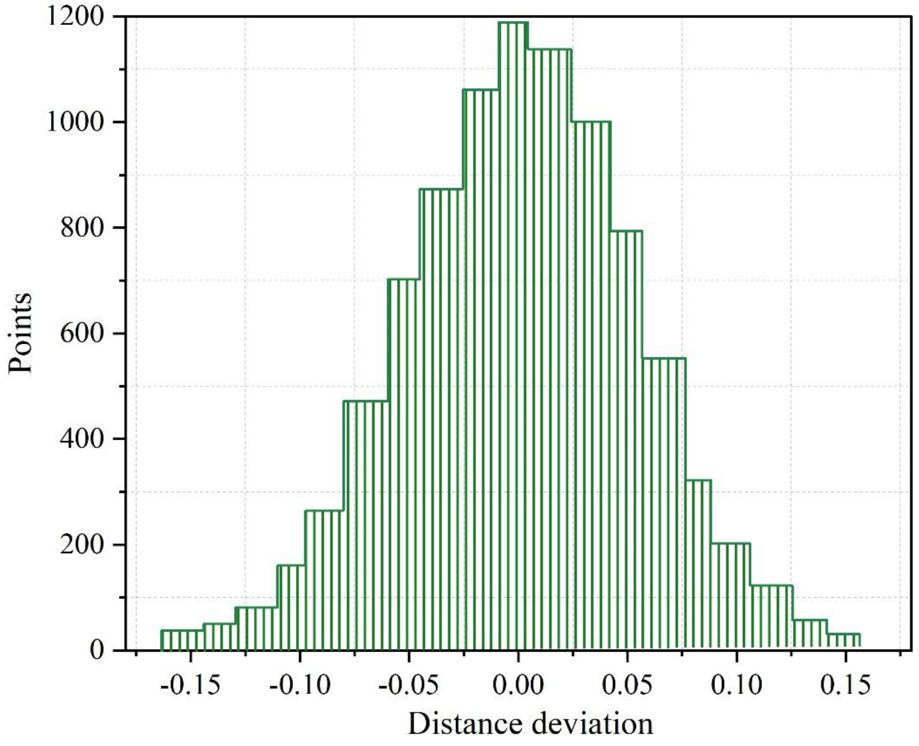

(a) Dot cloud 1

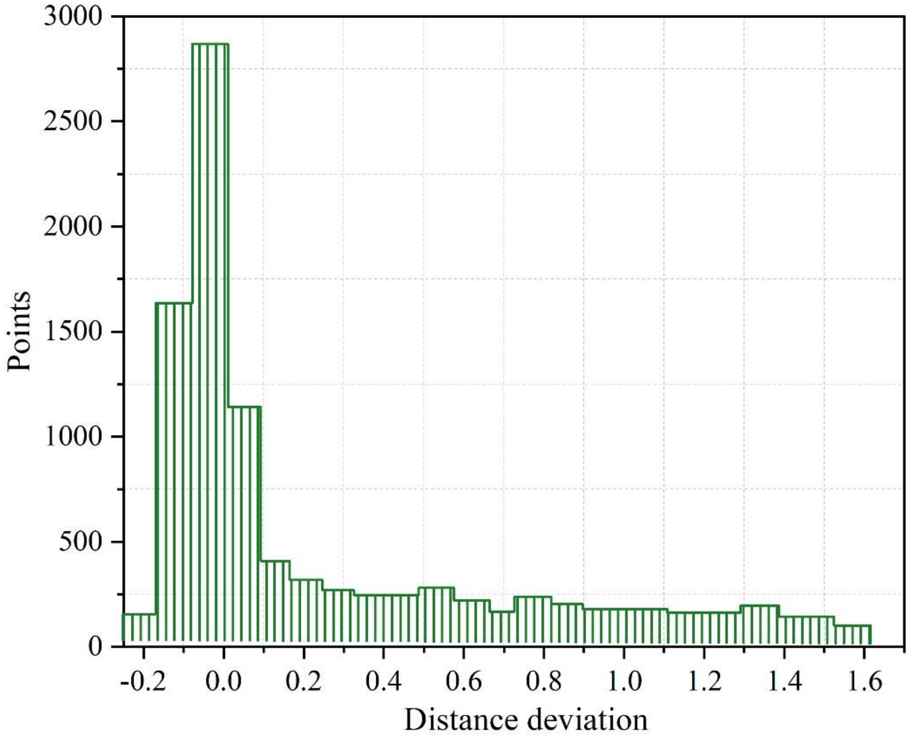

(b) Dot cloud 2

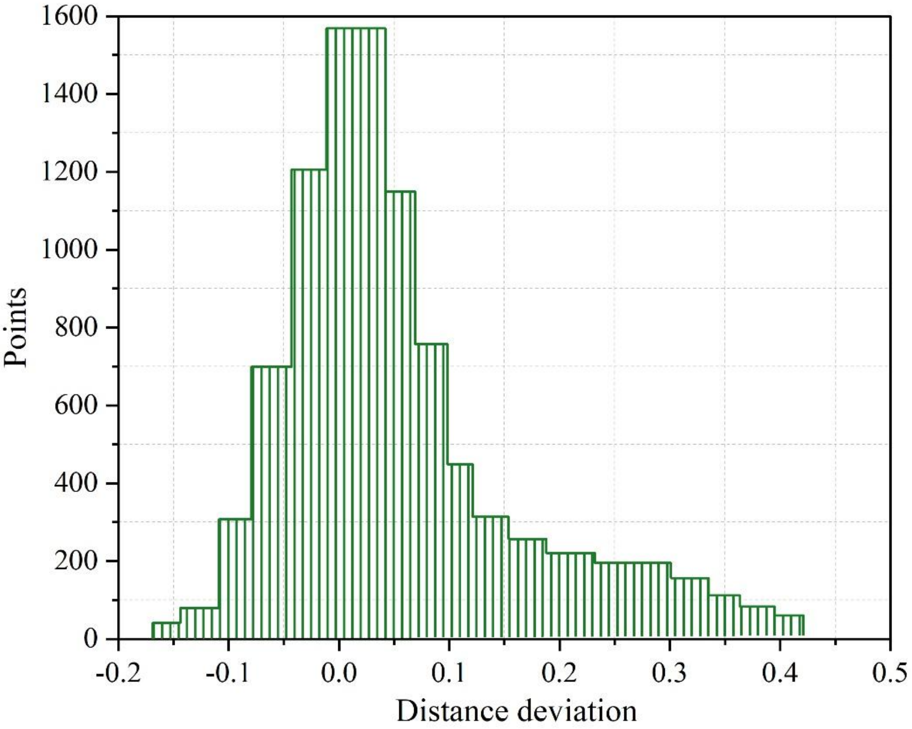

(c) Dot cloud 3

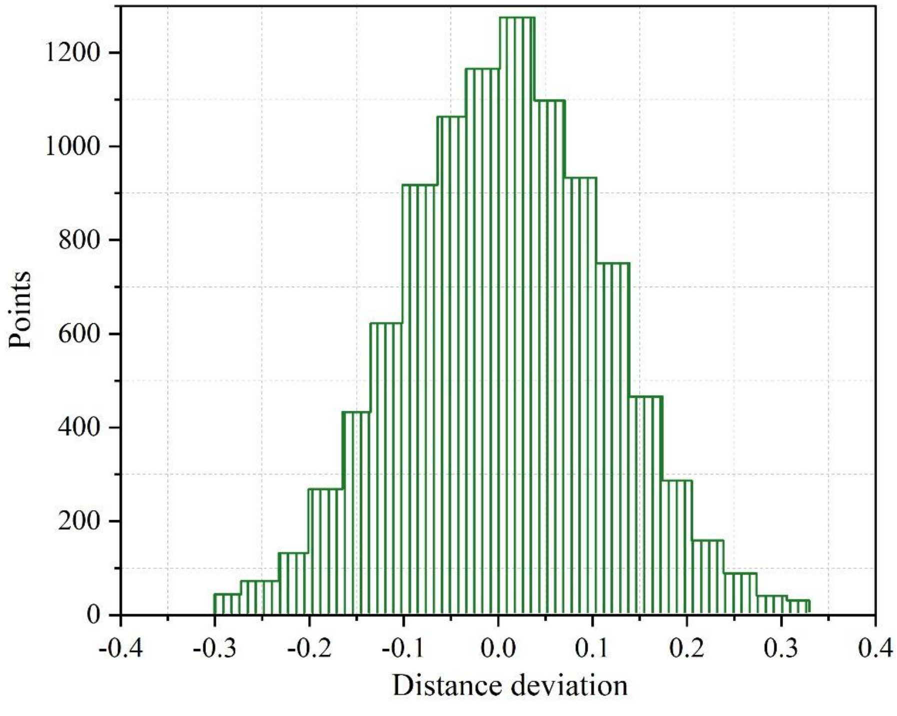

(d) Dot cloud 4

Figure 5. Model comparison test results.

The hypothesis test of normal distribution was performed on the four sets of test results with a pre-set significant level of α = 0.05, and the results of the model are shown in Table 3. In the hypothesis test statistic, it is compared to the critical value when the sample size is n. If $\chi^2 < \chi_\alpha^2$ then accept H_0

otherwise reject H_0. This is used to determine whether the hypothesis test is passed or not. As can be seen from the table, group 2 and group 3 with protruding deformation cannot pass the hypothesis test, regardless of the size of the deformation will change the normal distribution of the test, the method has a strong sensitivity to the changes in the distribution of errors caused by machining errors; group 1 and group 4 did not deform, but the machining accuracy is different; group 4 is more rough, assuming that the parts are given a tolerance of 0.18 mm. the use of tolerance bounds test method Accuracy evaluation is carried out, in which the $|3\sigma| = 0.1326 \leq 0.18$ parts of group 1 are qualified; the $|3\sigma| = 0.2519 > 0.18$ of group 4, the parts are unqualified. The test results show that the error inspection and machining accuracy evaluation method proposed in this paper can realize quantitative machining accuracy evaluation, and can be used for automatic screening of qualified batch of parts.

Table 3. Test results of the model.

Group	Point number	Pre-added random noise standard deviation	Hypothesis test results		Qualified decision	
			Standard deviation	Statistic	Critical value	Test result
1	9882	0.0405	0.0487	29.543	32.23	Pass
2	10066	0.0423	0.4289	15816.74	32.23	Unpassed
3	9906	0.0431	0.1038	3082.93	32.23	Unpassed
4	9974	0.0884	0.1087	19.161	32.23	Pass

4. Conclusion

This paper proposes a three-dimensional point cloud data alignment of mechanical workpiece deformation identification method to solve the problem of three-dimensional scanning data analysis in machining inspection.

(1) The algorithm in this paper has strong robustness to the scanning points of the machining error parts, and the alignment calculation will not let the machining error spread to the error-free parts. By comparing with the traditional method, the selection of weights in this paper can achieve more accurate alignment results, and effectively solve the problem of accurate alignment of point clouds with local deformation.

(2) The three index values of "AP50, AP75 and mAP" of the alignment algorithm in this paper reach 95.52%, 84.98% and 90.41% respectively. Compared with other target detection algorithms, there is a significant improvement, which can effectively solve the problem of three-dimensional data scanning and detection in machining.

(3) The method in this paper can realize quantitative machining accuracy evaluation, which can be used for batch and automatic screening of qualified parts in machining inspection.

References

1. Teng, C., Pal, D., Gong, H., Zeng, K., Briggs, K., Patil, N., & Stucker, B. (2017). A review of defect modeling in laser material processing. Additive Manufacturing, 14, 137-147.
2. Niu, P., Cheng, Q., Chang, W., Song, X., & Li, Y. (2021). Sensitivity analysis of machining accuracy reliability considering partial correlation of geometric errors for horizontal machining center. Proceedings of the Institution of Mechanical Engineers, Part B: Journal of Engineering Manufacture, 235(3), 455-465.
3. Wenqi, W. A. N. G., Wei, L. I. U., Zhang, Y., Yang, L. I. U., Zhang, P., & Zhenyuan, J. I. A. (2024). Precise measurement of geometric and physical quantities in cutting tools inspection and condition monitoring: A review. Chinese Journal of Aeronautics, 37(4), 23-53.
4. Farooq, M. A., Kirchain, R., Novoa, H., & Araujo, A. (2017). Cost of quality: Evaluating cost-quality trade-offs for inspection strategies of manufacturing processes. International Journal of Production Economics, 188, 156-166.
5. Park, M., & Jeong, J. (2022). Design and implementation of machine vision-based quality inspection system in mask manufacturing process. Sustainability, 14(10), 6009.
6. Psarommatis, F., May, G., Azamfirei, V., & Konstantinidis, F. (2024). Optimizing efficiency and zero-defect manufacturing with in-process inspection: Challenges, benefits, and aerospace application. Procedia Computer Science, 232, 2857-2866.
7. Genta, G., Galetto, M., & Franceschini, F. (2020). Inspection procedures in manufacturing processes: recent studies and research perspectives. International Journal of Production Research, 58(15), 4767-4788.

8. Aust, J., & Pons, D. (2022). Comparative analysis of human operators and advanced technologies in the visual inspection of aero engine blades. Applied Sciences, 12(4), 2250.
9. Tsuzuki, R. (2022). Development of automation and artificial intelligence technology for welding and inspection process in aircraft industry. Welding in the World, 66(1), 105-116.
10. Li, Y., Yu, B., Wang, B., Lee, T. H., & Banu, M. (2020). Online quality inspection of ultrasonic composite welding by combining artificial intelligence technologies with welding process signatures. Materials & Design, 194, 108912.
11. Zhang, Z., Li, J., Lu, L., Wang, Z., Liang, X., & Zhang, Y. (2025). Intelligent modeling and detection in grinding: a review of advances, challenges, and prospects. The International Journal of Advanced Manufacturing Technology, 1-61.
12. Martinez, P., Al-Hussein, M., & Ahmad, R. (2020). Intelligent vision-based online inspection system of screw-fastening operations in light-gauge steel frame manufacturing. The International Journal of Advanced Manufacturing Technology, 109(3), 645-657.
13. Chen, M. C., Yen, S. Y., Lin, Y. F., Tsai, M. Y., & Chuang, T. H. (2025). Intelligent Casting Quality Inspection Method Integrating Anomaly Detection and Semantic Segmentation. Machines, 13(4), 317.
14. Liu, Y., Duan, S., Shen, Z., He, Z., & Li, L. (2023). Grasp and inspection of mechanical parts based on visual image recognition technology. Journal of Theory and Practice of Engineering Science, 3(12), 22-28.
15. Martínez, S. S., Vázquez, C. O., García, J. G., & Ortega, J. G. (2017). Quality inspection of machined metal parts using an image fusion technique. Measurement, 111, 374-383.
16. Lin, X., Wang, X., & Li, L. (2020). Intelligent detection of edge inconsistency for mechanical workpiece by machine vision with deep learning and variable geometry model. Applied Intelligence, 50(7), 2105-2119.
17. Yang, T., Yi, X., Lu, S., Johansson, K. H., & Chai, T. (2021). Intelligent manufacturing for the process industry driven by industrial artificial intelligence. Engineering, 7(9), 1224-1230.
18. Sundaram, S., & Zeid, A. (2023). Artificial intelligence-based smart quality inspection for manufacturing. Micromachines, 14(3), 570.
19. Aggour, K. S., Gupta, V. K., Ruscitto, D., Ajdelsztajn, L., Bian, X., Brosnan, K. H., ... & Vinciquerra, J. (2019). Artificial intelligence/machine learning in manufacturing and inspection: A GE perspective. MRS Bulletin, 44(7), 545-558.
20. Kandi, H., Jain, A., Velluva Chathoth, S., Mishra, D., & Subrahmanyam, G. R. S. (2019). Incorporating rotational invariance in convolutional neural network architecture. Pattern Analysis and Applications, 22, 935-948.
21. Rajan, A. J., Jayakrishna, K., Vignesh, T., Chandradass, J., & Kannan, T. T. M. (2021). Development of computer vision for inspection of bolt using convolutional neural network. Materials Today: Proceedings, 45, 6931-6935.
22. Cheng, B., Li, Z., Wu, Q., Li, B., Yang, H., Qing, L., & Qi, B. (2019). Multi-class objects detection method in remote sensing image based on direct feedback control for convolutional neural network. IEEE Access, 7, 144691-144709.
23. Božič, A., Kos, M., & Jezeršek, M. (2020). Power control during remote laser welding using a convolutional neural network. Sensors, 20(22), 6658.
24. Terzić, S., Dedić, J., Lazarević, D., Šarkoćević, Ž., & Nedic, B. (2018). Machining contact and non-contact inspection technologies in industrial application. Journal of Production Engineering, 55-60.
25. Shen, Y., Ren, J., Huang, N., Zhang, Y., Zhang, X., & Zhu, L. (2023). Surface form inspection with contact coordinate measurement: a review. International Journal of Extreme Manufacturing, 5(2), 022006.
26. Meng, Z., Cui, X., Jiang, L., & He, X. (2019, June). Gear Inspection and Error Compensation Control Method Based on Coordinate Measuring Machine. In 2019 14th IEEE Conference on Industrial Electronics and Applications (ICIEA) (pp. 2393-2398). IEEE.
27. Kim, J., Choi, S., Choi, J., Lim, D., & Kim, J. (2020, October). Contact Type Thread Tester for Tap Inspection Automation. In 2020 20th International Conference on Control, Automation and Systems (ICCAS) (pp. 457-462). IEEE.
28. Dong, Z., Sun, X., Liu, W., & Yang, H. (2018). Measurement of free-form curved surfaces using laser triangulation. Sensors, 18(10), 3527.
29. Li, J., Zhou, Q., Li, X., Chen, R., & Ni, K. (2019). An improved low-noise processing methodology combined with PCL for industry inspection based on laser line scanner. Sensors, 19(15), 3398.
30. Lee, Y. C., Wu, Y. C., & Yeh, S. S. (2021). Development of an On-Machine External Thread Measurement System for CNC Lathes Using Eye-in-Hand Machine Vision with Morphology Technology. Engineering Letters, 29(3).
31. Kiran, M. B. (2022). A Novel Technique for the Surface Texture Inspection of Electrical Discharge Machined Surfaces Using Vision System. In Recent Advances in Mechanical Infrastructure: Proceedings of ICRAM 2021 (pp. 211-218). Singapore: Springer Nature Singapore.
32. Wang, F., Ho, S. C. M., & Song, G. (2019). Modeling and analysis of an impact-acoustic method for bolt looseness identification. Mechanical Systems and Signal Processing, 133, 106249.
33. Harishyam, B., Jenarthanan, M. P., Rishivanth, R., Rajesh, R., & Girish, N. S. (2023). Visual inspection of mechanical components using visual imaging and machine learning. Materials Today: Proceedings, 72, 2557-2563.
34. Wen, S., Chen, Z., & Li, C. (2018). Vision-based surface inspection system for bearing rollers using convolutional neural networks. Applied Sciences, 8(12), 2565.

35. Xuan Ding,Shen Chen,Mu Duan,Jinchang Shan,Chao Liu & Chuli Hu. (2024). Towards 3D Reconstruction of Multi-Shaped Tunnels Utilizing Mobile Laser Scanning Data. Remote Sensing,16(22),4329-4329.
36. Yusheng Zang,Changsheng Li,Jiajun Tang,Zhaoxiang Chen,Jianjun Ding,Shuming Yang & Zhuangde Jiang. (2025). A composite surface registration method for freeform surface evaluation based on ICP coarse registration and PSO fine registration. Optics and Lasers in Engineering,193,109079-109079.
37. Qi Xin & Zhengwei He. (2020). Three dimensional stratum interpolation and visualization based on section and borehole data from jointing the moving least square method and poisson reconstruction method. Earth Science Informatics,13(4),1-9.
38. Lin Lei & Yun Huang. (2025). Optimizing Visual Transformer and Faster R-CNN Integration for Efficient Object Detection. International Journal of Pattern Recognition and Artificial Intelligence,39(06).